

# Formation of Neptunium(V) Carbonates: Examining the Forceful Influence of Alkali and Alkaline Earth Cations

Anastasiia S. Kuzenkova, Tatiana V. Plakhova,\* Iurii M. Nevolin, Elizaveta S. Kulikova, Alexander L. Trigub, Vasily O. Yapaskurt, Maria D. Shaulskaya, Dmitry M. Tsybarendko, Anna Yu. Romanchuk, and Stepan N. Kalmykov



Cite This: <https://doi.org/10.1021/acs.inorgchem.3c02737>



Read Online

ACCESS |



Metrics & More

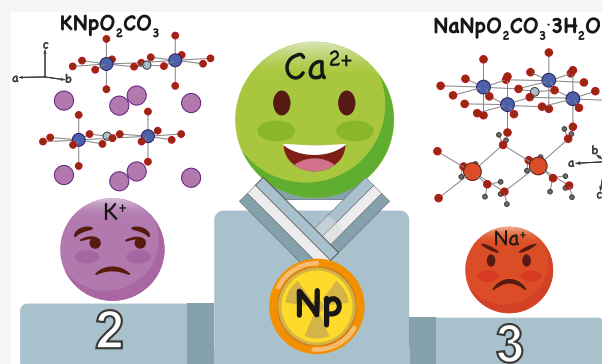


Article Recommendations



Supporting Information

**ABSTRACT:** Herein, neptunium(V) carbonates containing sodium or potassium cations were synthesized via chemical precipitation. Various techniques such as scanning electron microscopy, energy-dispersive X-ray spectroscopy, thermogravimetry combined with differential scanning calorimetry, X-ray diffraction, and X-ray absorption spectroscopy were used to analyze the microstructures and elemental compositions of these samples. The crystal structures of hydrated  $\text{NaNpO}_2\text{CO}_3 \cdot 3\text{H}_2\text{O}$  ( $P1$ ,  $a = 4.3420(2)$  Å,  $b = 4.8962(2)$  Å,  $c = 10.0933(11)$  Å,  $\alpha = 91.014(7)^\circ$ ,  $\beta = 77.834(11)^\circ$ , and  $\gamma = 90.004(10)^\circ$ ) and  $\text{KNpO}_2\text{CO}_3$  ( $P6_3/mmc$ ,  $a = b = 5.0994(2)$  Å,  $c = 10.2210(15)$  Å) were determined for the first time using the Rietveld method. The synthesized carbonates exhibited distinct structural features and decomposition behaviors, as demonstrated through thermogravimetry analysis, which revealed the presence of crystalline hydrate water in sodium neptunium(V) carbonate. Furthermore, calcium-containing neptunium(V) carbonates were synthesized and characterized. Samples with the general composition  $\text{Ca}_{0.5}\text{NpO}_2\text{CO}_3$  were obtained using the ion exchange method and chemical precipitation from solutions containing competing cations ( $\text{Ca}^{2+}$ ,  $\text{Na}^+$ ,  $\text{K}^+$ , and  $\text{Mg}^{2+}$ ). The synthesis conditions notably affected the diffraction patterns of the obtained calcium neptunium(V) carbonates. This investigation enhances our understanding of the structural properties and thermodynamic stability of neptunium(V) carbonates in the presence of diverse cations commonly found under radioactive waste disposal conditions.



## INTRODUCTION

Nuclear power generation yields a long-term radioactive waste challenge, necessitating their secure storage for centuries.<sup>1,2</sup> Countries with developed nuclear power industries are concerned about creating reliable and protected storage facilities for high-level wastes. Various host rock concepts for deep geological waste disposal have been proposed.<sup>3</sup> However, the potential intrusion of water in the near-field of a nuclear waste repository may mobilize radionuclides via aqueous pathways.<sup>4,5</sup> Thus, understanding radionuclide behavior in solutions is pivotal for safety analysis and performance assessment in the final disposal of nuclear waste in deep geological repositories.<sup>6–8</sup>

<sup>237</sup>Np is among the most dangerous radionuclides owing to its long half-life ( $T_{1/2} = 2.144 \times 10^6$  years) and high radiotoxicity as it is an  $\alpha$  emitter.<sup>9</sup> Spent nuclear fuel contains <1% of Np; however, <sup>237</sup>Np contribution to long-term waste activity grows owing to the increased Np content in nuclear waste from <sup>241</sup>Am decay over 5000 years. Under oxidizing conditions, as envisioned with oxygenated groundwater contacting the wastes, Np may dissolve as mobile  $\text{Np}^{(\text{V})}\text{O}_2^+$

species.<sup>10,11</sup> To predict the maximum Np mobilization from a waste repository through aqueous pathways, understanding the composition and properties of solubility-controlling Np phases and their solubility product constants ( $K_{\text{sp}}$ ) is vital.<sup>12–16</sup> Np speciation in solution is affected by local geochemistry, including the nature and concentrations of aqueous system components such as complexing ligands, redox-active species, or dissolved background electrolyte ions.

Np(V) has a high affinity for carbonate ions in the solid phase.<sup>17</sup> Np mixed carbonates are formed in the presence of alkali and alkaline earth metal cations. Initial discussion on Np chemistry in carbonate media dates back to the 1950s and 1960s, with the earliest studies describing the preparation of hydrated  $\text{KNpO}_2\text{CO}_3$  through chemical precipitation in

**Received:** August 7, 2023

**Revised:** November 22, 2023

**Accepted:** November 22, 2023

$\text{K}_2\text{CO}_3$  media.<sup>18,19</sup> The structures and composition of  $\text{M}^{(\text{I})}\text{NpO}_2\text{CO}_3$  ( $\text{M}(\text{I}) = \text{Cs}^+, \text{Rb}^+, \text{NH}_4^+, \text{K}^+, \text{Na}^+, \text{and Li}^+$ ) compounds have been revealed through thermogravimetric analysis and laboratory X-ray diffraction (XRD).<sup>20–25</sup> Depending on the alkali cation radius,  $\text{M}^{(\text{I})}\text{NpO}_2\text{CO}_3$  phases with different crystalline structures could be formed.  $\text{KNpO}_2\text{CO}_3$  crystallizes in a hexagonal crystal family similar to pentavalent Pu and Am carbonates.<sup>18,22</sup>  $\text{NH}_4\text{NpO}_2\text{CO}_3$  crystallizes in the same hexagonal crystal family.<sup>23,24</sup> Volkov et al. studied Np(V) carbonates with various M(I) cations in the structure,<sup>20–22,26–28</sup> highlighting morphotropic transformations from hexagonal to orthorhombic crystal structure as one moves from K to Na in the series of pentavalent Np monocarbonates with  $\text{Cs}^+, \text{Rb}^+, \text{NH}_4^+, \text{K}^+, \text{Na}^+, \text{and Li}^+$ . Although structural data for  $\text{NaNpO}_2\text{CO}_3$  are obtained from powder diffraction patterns, the refinement of its crystal group  $Pm2_1n$  and atom positions was limited to anhydrous  $\text{NaNpO}_2\text{CO}_3$ .<sup>21</sup> To the best of our knowledge, hydrated  $\text{NaNpO}_2\text{CO}_3 \cdot x\text{H}_2\text{O}$  structures lack reliable structure data, despite evidence indicating that different amounts of water molecules in the  $\text{NaNpO}_2\text{CO}_3 \cdot x\text{H}_2\text{O}$  structure could considerably change the position of the primary diffraction reflections.<sup>20</sup>

To estimate the Np concentration in an aqueous solution equilibrated with solids, understanding the solubility of different Np-containing solid phases is essential. Thermodynamic data exist for  $\text{M}^{(\text{I})}\text{NpO}_2\text{CO}_3$  compounds. Maya first proposed a reliable  $K_{\text{sp}}$  value for hydrated  $\text{NaNpO}_2\text{CO}_3(\text{s})$  in a 1 M  $\text{NaClO}_4$  aqueous solution.<sup>29</sup> Lemire et al. determine the solubility of hydrated  $\text{NaNpO}_2\text{CO}_3$  and  $\text{KNpO}_2\text{CO}_3$  at different temperatures.<sup>30</sup> The  $K_{\text{sp}}$  values of hydrated  $\text{NaNpO}_2\text{CO}_3$  and  $\text{Na}_3\text{NpO}_2(\text{CO}_3)_2$  at various ionic strengths were determined by Neck et al.<sup>31</sup> Vitova et al. observed the preferential precipitation of K-solid phases of Np(V) over Na when K and Na concentrations were comparable.<sup>32</sup>

However, limited information is available on the structure and thermodynamic data of Np(V) carbonates mixed with divalent cations with the general formula  $\text{M}^{(\text{II})}_{0.5}\text{NpO}_2\text{CO}_3$  ( $\text{M}(\text{II}) = \text{Mg}^{2+}, \text{Ca}^{2+}, \text{Sr}^{2+}, \text{Ba}^{2+}, \text{etc.}$ ). The potential formation of  $\text{M}^{(\text{II})}_{0.5}\text{NpO}_2\text{CO}_3$  via ion exchange with the hydrated  $\text{NaNpO}_2\text{CO}_3$  phase has been previously reported.<sup>26</sup> However, detailed characterizations of the reaction products and other studies investigating similar phases are notably scarce. These compounds can play an essential role in Np migration, especially in repository-relevant systems where  $\text{Mg}^{2+}$  and  $\text{Ca}^{2+}$  are common background electrolyte ions, alongside  $\text{Na}^+, \text{K}^+$ , and  $\text{Cl}^-$  ions.<sup>13</sup>

Thus, enhancing the reliability of structural information for  $\text{M}^{(\text{I})}\text{NpO}_2\text{CO}_3$  compounds is essential. Moreover, comprehensive elucidation of the synthesis methods for  $\text{M}^{(\text{II})}_{0.5}\text{NpO}_2\text{CO}_3$  compounds, with the scarcity of available structural information being pronounced in this case, is in demand. This work aimed to synthesize and characterize the  $\text{M}^{(\text{I})}\text{NpO}_2\text{CO}_3$  ( $\text{M}^{(\text{I})} = \text{Na}^+ \text{ and } \text{K}^+$ ) structure and explore the potential formation of similar phases with divalent cations. The synthesis of alkali-mixed Np(V) carbonates involved the chemical precipitation of Np(V) in carbonate solutions containing Na and K. The Ca-containing Np(V) carbonate phases were obtained using different synthesis routes. Synchrotron methods were used to study the local environment of Np atoms (extended X-ray absorption fine structure spectroscopy (EXAFS)) and long-range order of the samples (XRD). Synchrotron radiation offered high signal-to-noise data

from small sample quantities, which is especially important when working with radioactive samples. Scanning electron microscopy (SEM) was used to investigate the sample morphology and local elemental composition. This combination of methods yielded reliable structural information for hydrated  $\text{M}^{(\text{I})}\text{NpO}_2\text{CO}_3$  and  $\text{M}^{(\text{II})}_{0.5}\text{NpO}_2\text{CO}_3$  compounds.

## MATERIALS AND METHODS

**Caution!**  $^{237}\text{Np}$  is a radioactive isotope and an  $\alpha$ -emitter. Radioactive samples were handled in specialized facilities equipped to mitigate the potential health hazards associated with radiation exposure.

**Synthesis.** All solutions were prepared by using ultrapure water from a Milli-Q (Millipore) apparatus. The Np source used was  $\text{NpO}_2$ , which was dissolved in concentrated nitric acid. Subsequently, Np was oxidized in concentrated  $\text{HClO}_4$  at 200 °C. To stabilize Np(V) in the solution, aliquots of a 0.1 M  $\text{NaNO}_2$  solution were added to a stock solution at room temperature. Ultraviolet–visible (UV–vis) spectroscopy (UV-1900i, Shimadzu) confirms the final pentavalent Np oxidation state, which shows characteristic peaks at 979, 616, and 475 nm (Figure S1). Liquid scintillation counting with  $\alpha$ – $\beta$  discrimination determined the  $^{237}\text{Np}$  concentration in the stock solution (Quantulus GCT 6220, PerkinElmer).

Samples labeled A–D were synthesized to obtain Np carbonates with Na and K. Sample A was synthesized from an Np(V) solution with a concentration of  $2 \times 10^{-3}$  M by adding  $\text{NaHCO}_3$  and  $\text{NaOH}$  to reach a pH of 8.8. Samples B–D were synthesized from Np(V) solution with an initial concentration of  $4 \times 10^{-3}$  M under a pH range of 7–8. During the synthesis of these three samples,  $\text{K}^+$  and  $\text{Na}^+$  were present in the initial solution, together with Np. The exact concentrations of  $[\text{Na}^+]$  and  $[\text{K}^+]$  in the synthesis and the pH values are listed in Table S1.

Several synthesis procedures were used to obtain Ca-mixed Np carbonates (Samples E–G). Sample E was prepared using an ion exchange method, where Sample D was immersed in a 0.1 M  $\text{CaCl}_2$  solution for 3 days. Once a day, the solid phase was separated via centrifugation for matrix solution update. Np concentration in the solution was controlled during the synthesis to confirm the absence of phase dissolution. The final solid phase was further characterized. Sample F was obtained via precipitation from a solution containing 0.005 M Np(V) in 0.05 M  $\text{CaCl}_2$  solution with a pH of 8 achieved by adding  $\text{NaOH}$ . To prepare Sample G, an aliquot of the Np(V) stock solution was added to a simulated natural hard water solution with a predominant concentration of Ca (Table S1). The pH of the resulting mixture was set to 8 using  $\text{NH}_3 \cdot \text{H}_2\text{O}$ .

All syntheses were conducted under oxidic conditions at 25 °C. The colors of the resulting samples varied from white to dark blue depending on the synthesis condition. Glass combination electrodes (InLab Semimicro, Mettler Toledo) calibrated with standard pH buffers were used to determine the pH of the solutions. Redox potentials  $E(\text{mV})$  were measured with a Pt electrode relative to an Ag/AgCl reference electrode, and the results were converted to Eh ( $\text{Eh}(\text{mV}) = E(\text{mV}) + 208 \text{ mV}$ ). The Eh values were directly measured in the Np-containing suspensions, and measurements were performed until the Eh value remained stable within 5 mV over 30 min. During the syntheses, the redox potential was within 0.58–0.70 V (Eh vs HSE). According to the Pourbaix diagram, these redox conditions correspond to Np(V) in solution, as shown in Figure S2. Before characterization, all solid phases were washed 1 to 2 times with Milli-Q water to remove residual reagents.

**X-ray Diffraction.** Synchrotron XRD data for Np-containing samples were collected at the XSA beamline<sup>33</sup> of the Kurchatov Synchrotron Radiation Source (Moscow, Russia) using a Rayonix SX165 detector. Diffraction patterns were obtained by using monochromatic radiation (wavelength = 0.75 Å) focused on a 400  $\mu\text{m}$  spot of the sample held in a quartz capillary. The exact wavelength of the monochromatic radiation was specified before the experiments using  $\text{LaB}_6$  standard calibration.

To obtain XRD data for phase analysis, the intensity vs scattering angle patterns were derived from two-dimensional (2D) patterns

using the Dionis software,<sup>34</sup> and the signal from an empty capillary was extracted as a background reference. XRD patterns for Samples A and D, utilized for structure solution and refinement, were obtained by processing 2D frames using Dioptas v.0.5.0 software<sup>35</sup> calibrated with a LaB<sub>6</sub> reference sample. The patterns were *ab initio* indexed using the dichotomy method<sup>36</sup> and LSI-index algorithm.<sup>37</sup> Full profile refinement with le Bail decomposition to extract structure factors and subsequent Rietveld refinement were performed within JANA2006 software.<sup>38</sup>

The refined unit cell parameters and the overall XRD pattern of Sample D closely resembled those of the KPuO<sub>2</sub>CO<sub>3</sub> analog.<sup>39</sup> The KPuO<sub>2</sub>CO<sub>3</sub> structure was used as a starting model for structure refinement by using the Rietveld method. In this process, the positions of O1 and O2 were refined, while other atoms were placed at special positions. K and Np were refined with anisotropic thermal parameters, while other atoms were treated isotropically.

The crystal structure of Sample A was determined *ab initio* within several stages. First, the charge flipping method in Jana2006<sup>38</sup> was applied to determine the position of Np1, C1, and O1–O5 within the NpO<sub>2</sub>CO<sub>3</sub> layer. Then, the partial structural model of Sample A was refined by using the Rietveld method with geometrical restraints. The positions of Na1 and O6–O8 in the interlayer space were obtained through Monte-Carlo simulation using FOX software<sup>40</sup> while keeping the layer geometry fixed. H atoms of H<sub>2</sub>O molecules were calculated geometrically. The final structural model was refined using the Rietveld method, incorporating one set of anisotropic thermal parameters for the O4=Np1=O5 group and three isotropic parameters for other atoms (one each for Na1, C1 and O1–O3 group, and O6–O8 group). Geometrical constraints were applied to maintain the linearity of the group of O4=Np1=O5 with equal Np–O distances and the planarity of the CO<sub>3</sub> group with similar C–O distances and O–C–O angles. After that, the unit cell showed neither any noticeable Fourier peaks nor free cavities that could be attributed to additional water molecules. Notably, the triclinic unit cell can be transformed by the matrix (−1, 0, 2, 1, 0, 0, 1, 0) into a C-centered pseudomonoclinic cell with refined cell parameters  $a = 19.7369(10)$  Å,  $b = 4.34242(9)$  Å,  $c = 4.89603(10)$  Å,  $\alpha = 90.010(4)^\circ$ ,  $\beta = 91.005(4)^\circ$ , and  $\gamma = 90.283(5)^\circ$ . Thus, the  $\gamma$  parameter remarkably deviated from 90°. Moreover, despite the nearly orthogonal symmetry of the NpO<sub>2</sub>CO<sub>3</sub> layer, describable in a monoclinic cell, the interlayer Na1 and H<sub>2</sub>O molecules break the symmetry; therefore, the overall structure of Sample A was refined in the triclinic unit cell.

**X-ray Absorption Spectroscopy.** X-ray absorption spectroscopy (XAS) data were collected at the Structural Materials Science beamline<sup>41</sup> of the Kurchatov Synchrotron Radiation Source (Moscow, Russia). A storage ring with an electron beam energy of 2.5 GeV and a current of 80–100 mA was used. Np L<sub>3</sub> edge XAFS was measured with a Si (220) channel-cut monochromator, yielding an energy resolution of  $\Delta E/E \approx 2 \times 10^{-4}$ . The suppression of high-energy harmonics was achieved through monochromator geometry distortions. Energy calibration was performed by using the XAFS spectrum of the Np(V) standard sample. As a standard sample, an aqueous solution of Np(V) with a concentration of 10<sup>−3</sup> M was used. All experimental data were collected in transmission mode using two ionization chambers, one filled with a mixture of Ar/N<sub>2</sub> (in a 2/3 ratio) and the other filled with Ar. At every energy point in the X-ray absorption near-edge structure (XANES) region, the signal was integrated for 1 s, with an energy step of 0.8 eV. In contrast, for the EXAFS region, the integration time was set to 1 s at the beginning of the region and increased to 4 s at the end of the region. Samples for Np L<sub>3</sub> measurements were held in polymer holders during the measurements. To monitor sample radiation damage, fast and long-time scans were compared in the XANES region, revealing no observable radiation damage. The beam size for Np L<sub>3</sub> XAS spectra was chosen to cover the homogeneous area of the samples, but it was not <500 μm × 500 μm to ensure an appropriate signal/noise ratio. At least three spectra were collected and merged for all samples using the IFEFFIT software.<sup>42</sup>

The EXAFS data analysis was first performed using the standard procedure implemented in IFEFFIT software.<sup>42</sup> The absolute value of

the Fourier transformed  $k^2$ -weighted oscillation component of the EXAFS function was fitted within an  $R$  range of 1.1–5.2 Å. The theoretical EXAFS function was expressed as a sum of partial contributions  $\chi_i$ , with each component calculated using the standard EXAFS equation

$$\chi_i(k) = S_0^2 \frac{N_i F_i(k)}{R_i^2 k} e^{-2R_i/\lambda(k)} e^{-2\sigma_i^2 k^2} \sin(2kR_i + \varphi_i(k))$$

where  $\lambda(k)$  is the photoelectron mean free path,  $F_i(k)$  is the amplitude, and  $\varphi_i(k)$  is the phase shift of scattered photoelectron wave calculated *ab initio* using the FEFF8<sup>43</sup> program based on atomic clusters derived from crystallographic structures determined through XRD experiments. Interatomic distances ( $R_i$ ), coordination numbers ( $N_i$ ), and Debye–Waller factors ( $\sigma^2$ ) were determined through nonlinear fitting of theoretical spectra to experimental data. The semiempirical amplitude reduction factor  $S_0^2$  considers many-body losses; after preliminary tests,  $S_0^2$  was fixed at 0.9 for all data analyses.

The reverse Monte Carlo (RMC) method is a simulation technique that provides the three-dimensional (3D) atomic structure of a material by minimizing the difference between experimental signals and a configuration-averaged theoretical curve calculated from the simulated atomic positions. The evolutionary algorithm of the RMC method was used for the EXAFS spectra fitting as implemented in the EvAX code.<sup>44</sup> A critical advantage of the RMC method is the automatic handling of multiple scattering (MS) paths. The inclusion of MS paths in conventional EXAFS fitting leads to a drastic increase in the number of fitted parameters, often compromising the result reliability. In EvAX, the configuration-averaged EXAFS signal  $\chi(k)$  is obtained using the *ab initio* real-space MS FEFF8 code,<sup>43</sup> embedded in the EvAX distribution. Experimental and theoretical spectra were compared in wavelet transform (WT) space. The minimization procedure was performed in the  $k^2$ -weighted WT,<sup>45</sup> considering a  $k$  range of 3–14 Å<sup>−1</sup> and  $R$  range of 1–6 Å. The RMC-EXAFS procedure was applied to a 5 × 5 × 2 supercell under periodic boundary conditions. The amplitude reduction factor  $S_0^2$  was fixed at 0.9 throughout the calculations. At each RMC iteration, new supercell configurations were generated by randomly displacing all atoms within the simulation box with a maximum displacement of 0.4 Å. Eight simulations were performed using different initial random seed numbers to obtain radial distribution functions (RDFs) with the appropriate statistics. The final EXAFS fit and RDF curves were calculated by averaging the results from all of these calculations.

**SEM and TG–DSC Measurements.** The morphology and chemical composition of the samples were studied using a Jeol JSM IT-500 SEM instrument with a tungsten thermionic cathode and equipped with an Oxford X-Max-n energy-dispersive spectrometer. The samples deposited on a silicon substrate were covered with 20–25 nm-thick conductive carbon films in a vacuum evaporator. Electron images in secondary and backscattered electrons (SEs and BSEs, respectively) and analytical measurements were conducted at an accelerating voltage of 20 kV. For energy-dispersive X-ray (EDX) analysis, the electron probe current was set at 0.7 nA, and the exposure time was 60 s. Detection thresholds for all analyzed elements were reached at concentrations of 0.1–0.2 wt %. The obtained spectra were processed using the INCA program (version 21b) with corrections according to the XPP model. The concentrations of unstable elements were calculated by using internal standards, while stable elements were analyzed by using standards of their simple stoichiometric compounds under identical measurement conditions for the standards and samples.

Thermogravimetry and differential scanning calorimetry (TG–DSC) measurements were performed using a Netzsch STA Jupiter 449 F3 thermoanalytical complex. Heating occurred at a rate of 5 °C/min within the temperature range of 40 to 1000 °C. Pt–Rh crucibles and Pt–Rh sample carriers were used, and the atmosphere was a N<sub>2</sub>–20% vol O<sub>2</sub> mixture with a purity of  $\omega$  (N<sub>2</sub> + O<sub>2</sub>) = 99.999%.

## RESULTS AND DISCUSSION

### Characterization of Na, K– Np Mixed Carbonates.

Sample A was obtained from Np(V) stock solution through chemical precipitation in a substantial excess of  $\text{NaHCO}_3$  ( $[\text{NpO}_2^+] = 2 \times 10^{-3}$  M and  $[\text{Na}^+] = 3 \times 10^{-1}$  M). The XRD pattern of Sample A is shown in Figure 1a. This sample has diffraction peaks similar to those found in previously reported mixed Na–Np carbonate  $\text{NaNpO}_2\text{CO}_3 \cdot x\text{H}_2\text{O}$ .<sup>20,31</sup> Samples B–D were synthesized to study the behavior of Np in the presence of competing  $\text{K}^+$  and  $\text{Na}^+$  ( $[\text{NpO}_2^+] = 2 \times 10^{-3}$  M,  $[\text{Na}^+] = 7 \times 10^{-2}$  M,  $[\text{K}^+] = 2 \times 10^{-2}$  M and pH = 7–8 under oxic conditions). These samples were characterized

through XRD, revealing their different diffraction patterns (Figure 1b). Sample D consists of a single phase, with its diffraction pattern closely resembling data published for the  $\text{KNpO}_2\text{CO}_3$  structure.<sup>18,19,27</sup> Conversely, Samples B and C contain two phases of Np carbonates with clearly distinguishable scattering reflections attributed to  $\text{NaNpO}_2\text{CO}_3 \cdot x\text{H}_2\text{O}$  and  $\text{KNpO}_2\text{CO}_3$  phases. Notably, Np in Na and K carbonate structures remains in the pentavalent state, as confirmed using the XANES spectra (Figure S3), which were compared to those of an Np(V) reference compound.

Despite K and Na-mixed Np carbonates have been reported to form under various conditions,<sup>20,30,32,46</sup> no reliable structural data and morphological characteristics exist for the compounds  $\text{NaNpO}_2\text{CO}_3 \cdot x\text{H}_2\text{O}$  and  $\text{KNpO}_2\text{CO}_3$ . Herein, the solids  $\text{KNpO}_2\text{CO}_3$  (Sample D) and  $\text{NaNpO}_2\text{CO}_3 \cdot x\text{H}_2\text{O}$  (Sample A) are analyzed by using multiple techniques to identify their morphology, crystal structure, and Np local coordination environments.

The SEM images of Samples A and D are displayed in Figure 2a,b. These images reveal large-scale, uniform, flower-like microstructures obtained under specific synthesis conditions. Close observation revealed that each flower-like structure consists of several plates aligned radially from a center point. The thickness of each plate is between 50 and 100 nm. EDX analysis conducted alongside SEM measurements confirmed the differences in the phase composition of Np precipitates. In Sample A, the EDX analysis revealed the presence of Na in the local elemental composition. The average Na/Np atomic ratio at various points in the sample confirmed the general formula for Sample A to be  $\text{NaNpO}_2\text{CO}_3$  (Table S2 and Figure S4a). For Sample D, EDX measurements revealed the presence of K, Na, and Np (Table S2 and Figure S4b). Synthesis residues in the sample can explain the presence of Na in some areas of Sample D. Notably, with SEM–EDX, detecting characteristic X-ray lines of K at a low concentration alongside intense Np lines can be challenging because of their substantial spectral overlap.

According to the TG–DSC data, the hydrated Na-containing Np(V) carbonate decomposes in two stages, starting at 98 °C (Figure 2c). The first stage exhibits a notable endothermic effect with a minimum at 115 °C, causing a 5.5% weight loss in the sample at 40–200 °C. The second stage begins at 395 °C, with intense decomposition accompanied by heat absorption with a minimum at 416 °C. At 200–500 °C, the observed weight loss for hydrated  $\text{NaNpO}_2\text{CO}_3$  is 9.8%. A pronounced drop in Sample A mass during the first stage of decomposition indicates the elimination of chemically bound water of crystallization. The second stage of the process likely involves the decomposition of the carbonate ion and the removal of  $\text{CO}_2$ , consistent with literature data.<sup>20</sup>

In contrast, the decomposition of the  $\text{KNpO}_2\text{CO}_3$  sample differs from that of the Na form (Figure 2d). Hardly any change in mass is observed for  $\text{KNpO}_2\text{CO}_3$  at 40–200 °C, with a reduction of <1% in weight. Fluctuations in heat flow occur during this temperature range but cannot be attributed to any specific process. Intensive decomposition of the sample begins at 493 °C. In this case, in the range of 200–600 °C, the weight loss of the sample is 11.7%. Unlike the Na analogue, the  $\text{KNpO}_2\text{CO}_3$  sample does not contain water of crystallization, evident from the lack of substantial weight loss at 40–200 °C. The slow weight decrease in this range results from the removal of sorbed  $\text{H}_2\text{O}$  molecules from the  $\text{KNpO}_2\text{CO}_3$

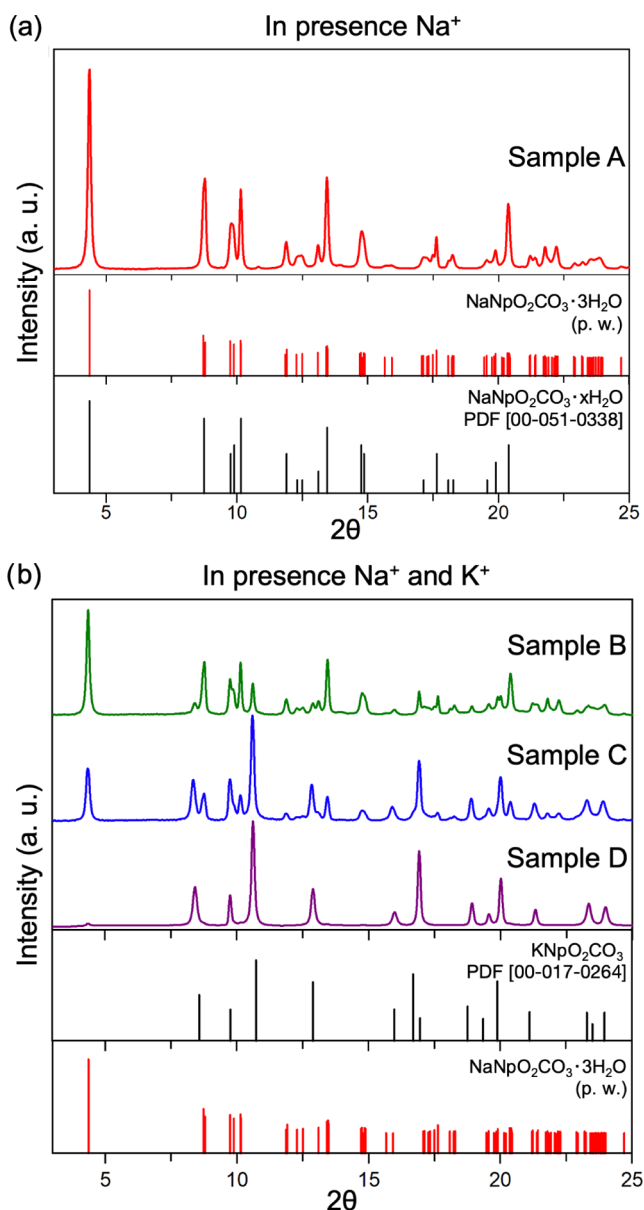


**Figure 1.** Synchrotron-based XRD patterns: (a) Comparison of Sample A obtained in the presence of  $\text{Na}^+$  with the literature data for  $\text{NaNpO}_2\text{CO}_3 \cdot x\text{H}_2\text{O}$  from Neck et al.<sup>31</sup> (ICDD PDF-4+ database) and with the structure  $\text{NaNpO}_2\text{CO}_3 \cdot 3\text{H}_2\text{O}$  refined in the present work (p.w.). (b) XRD patterns for Samples B, C, and D obtained in the presence of different  $\text{Na}^+$  and  $\text{K}^+$  concentrations, along with the literature data for  $\text{KNpO}_2\text{CO}_3$  from Keenan and Kruse work<sup>18</sup> (ICDD PDF-4+ database).

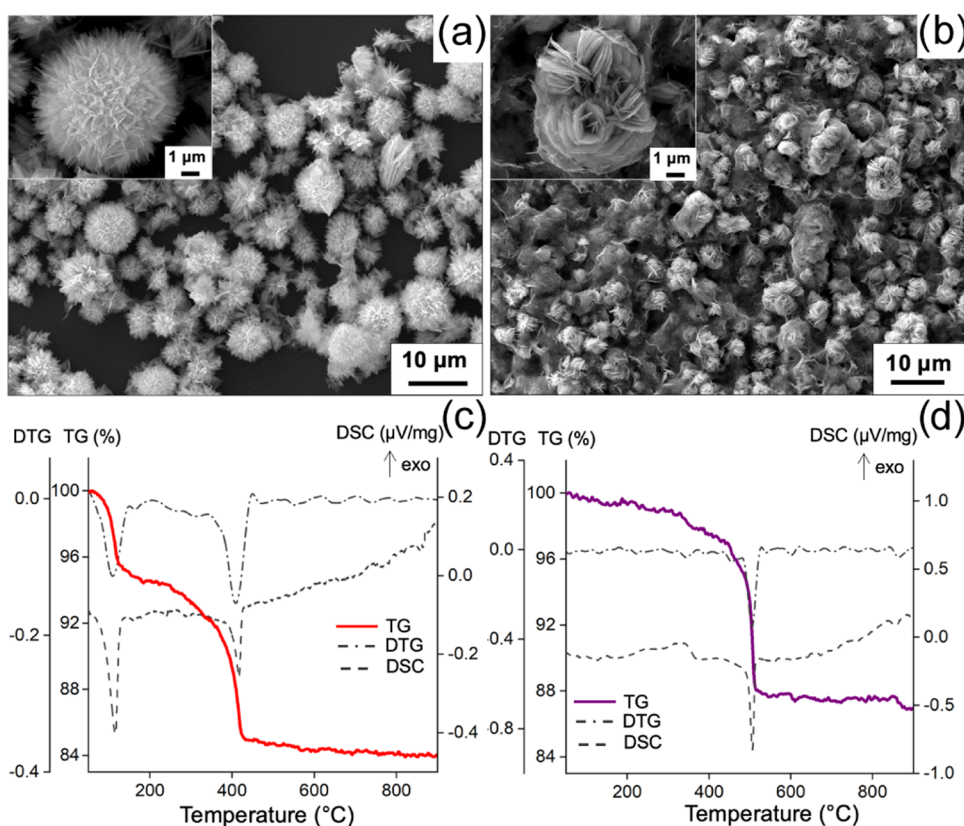


**Figure 2.** SEM images of (a) Sample A and (b) Sample D (insets: high-magnification images). TG–DSC data for (c) Sample A and (d) Sample D.

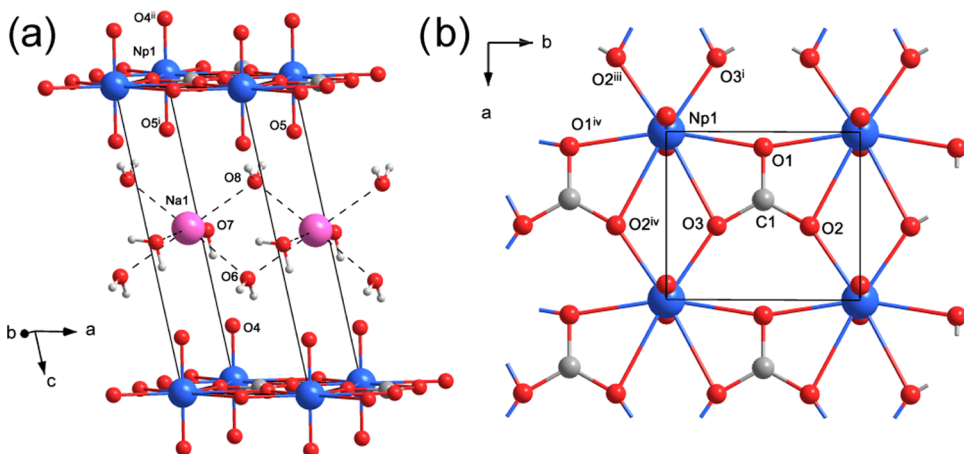


**Figure 3.** Crystal structure of  $\text{NaNpO}_2\text{CO}_3 \cdot 3\text{H}_2\text{O}$ : (a) unit cell comprising an anionic layer of neptunyl carbonate and a layer of hydrated  $\text{Na}^+$ ; (b) anionic layer within the  $ab$  plane. Symmetry codes: (i)  $-1 + x, y, z$ ; (ii)  $x, y, -1 + z$ ; (iii)  $-1 + x, -1 + y, z$ ; (iv)  $x, -1 + y, z$ .

sample. The weight loss at 200–600 °C is most likely caused by carbonate decomposition in the  $\text{KNpO}_2\text{CO}_3$  sample.

The crystal structures of Samples A and D were refined based on synchrotron XRD data (Table S3 and Figure S5). While there is a substantial lack of information about the possible structures of the hydrated form of Na-containing Np(V) carbonates, we discover the structure of hydrated  $\text{NaNpO}_2\text{CO}_3 \cdot 3\text{H}_2\text{O}$  for the first time. For Sample A, the experimental XRD data are best described using a model based on the structure with the general formula  $\text{NaNpO}_2\text{CO}_3 \cdot 3\text{H}_2\text{O}$  (Figure S5a), providing a more accurate description of reflections in Sample A compared to the literature<sup>31</sup> (Figure 1a). The proposed structure of  $\text{NaNpO}_2\text{CO}_3 \cdot 3\text{H}_2\text{O}$  exhibits a

layered structure with alternating anionic layers  $[\text{NpO}_2\text{CO}_3]_n^{n-}$  and the interlayer cationic species  $[\text{Na}(\text{H}_2\text{O})_3]_n^{n+}$  (Figure 3a). The anionic  $[\text{NpO}_2\text{CO}_3]_n^{n-}$  layer adopts a nearly orthorhombic structure similar to the layer geometry in the anhydrous  $\text{NaNpO}_2\text{CO}_3$ <sup>21</sup> (Figure 3b). Within this layer, Np1 and the carbonate anion (C1 and O1–O3) lie in the  $ab$  plane, while O4 and O5 atoms are located above and below the  $ab$  plane, creating a linear  $\text{O4}=\text{Np1}=\text{O5}$  neptunyl fragment that is perpendicular to the  $ab$  plane. The Np–O distance in the neptunyl  $\text{NpO}_2^+$  is 1.79(4) Å. The hydrated cationic species  $[\text{Na}(\text{H}_2\text{O})_3]_n^{n+}$  occupy the space between the anionic layers, where  $\text{Na}^+$  is enclosed in a distorted octahedron formed by three water molecules. These

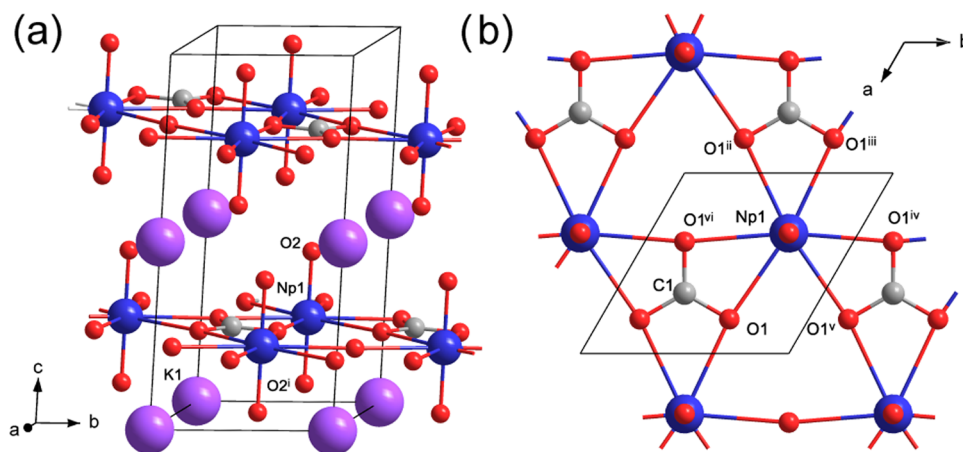


**Figure 4.** Crystal structure of  $\text{KNpO}_2\text{CO}_3$ : (a) unit cell containing anionic layers of neptunyl carbonate and  $\text{K}^+$ ; (b) anionic layer in the  $ab$  plane. Symmetry codes: (i)  $1 - y, 1 - x, 0.5 - z$ ; (ii)  $-1 + x, x - y, 0.5 - z$ ; (iii)  $-x + y, y, 0.5 - z$ ; (iv)  $1 - y, 1 + x - y, z$ ; (v)  $x, 1 + x - y, 0.5 - z$ ; (vi)  $1 - y, x - y, z$ .

layers are stacked parallel to each other with a pronounced mutual shift of  $[\text{NpO}_2\text{CO}_3]_n^{n-}$  layers by 2.13 along the  $a$ -axis only. This shift contrasts with the related anhydrous  $\text{NaNpO}_2\text{CO}_3$  layers, which are shifted along two directions by 2.18 and 2.43 and are inverted. The inclusion of water molecules into the structure considerably increases the interlayer separation from 5.34 to 10.09 Å. The interlayer atoms, Na1 and  $\text{H}_2\text{O}$  molecules, break the pseudomonoclinic metric symmetry of  $\text{NaNpO}_2\text{CO}_3 \cdot 3\text{H}_2\text{O}$ , resulting in a triclinic cell. Selected bond distances in the  $\text{NaNpO}_2\text{CO}_3 \cdot 3\text{H}_2\text{O}$  structure are presented in Table S4.

According to Volkov, the  $\text{NaNpO}_2\text{CO}_3 \cdot x\text{H}_2\text{O}$  can undergo reversible dehydration and ion exchange reactions that impact its diffraction pattern,<sup>20</sup> which led to the hypothesis that water molecules are not directly associated with Np in the structure. Instead, hydrated forms are thought to arise through the interlayer water molecules. Our experimental results confirm Volkov's assumptions. The structures of the anionic layers  $[\text{NpO}_2\text{CO}_3]_n^{n-}$  in both anhydrous  $\text{NaNpO}_2\text{CO}_3$  and  $\text{NaNpO}_2\text{CO}_3 \cdot 3\text{H}_2\text{O}$  coincide, and the transition from anhydrous carbonate to tetrahydrate increases the anion interlayer distance and causes its shift.

For Sample D, the experimental XRD data best correspond to the hexagonal  $\text{KNpO}_2\text{CO}_3$  structure (Figure S5b). This compound  $\text{KNpO}_2\text{CO}_3$  crystallizes in space group  $P6_3/mmc$ , featuring a hexagonal structure comprising  $[\text{NpO}_2\text{CO}_3]$  layers with  $\text{K}^+$  located between the layers (Figure 4). Our findings corroborate with the information regarding the space group and unit cell parameters for  $\text{KNpO}_2\text{CO}_3$  provided in the Keenan and Kruse study,<sup>18</sup> where they refined the  $\text{KNpO}_2\text{CO}_3$  crystal system based on powder diffraction and chemical titration results. Herein, synchrotron XRD allowed us to refine the space group and lattice parameters, present a reliable structure model, and refine interatomic distances for the  $\text{KNpO}_2\text{CO}_3$  compound (Table S5).

The structures proposed from XRD were used to perform experimental EXAFS spectral fitting procedures. These spectra show different local surroundings of Np in the structures of Na- and K-containing Np carbonates (Figure 5). The RMC analysis was applied to extract structural information from the EXAFS spectra. Conventional EXAFS data analysis used for symmetrical molecular or crystalline systems encounters limitations in accounting for MS paths, owing to restricted

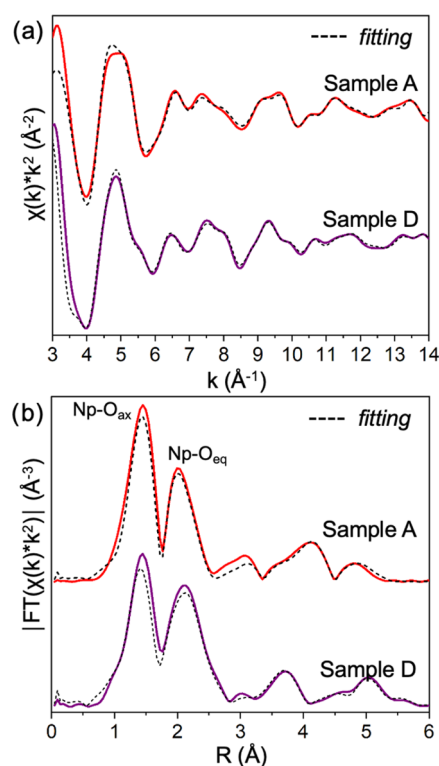


**Figure 5.** Np  $L_3$ -EXAFS  $R$ -space fitting results for (a, b)  $\text{NaNpO}_2\text{CO}_3 \cdot x\text{H}_2\text{O}$  (Sample A) and (c, d)  $\text{KNpO}_2\text{CO}_3$  (Sample D). The colored solid lines indicate the Fourier transform magnitude of EXAFS data, while the dashed lines represent the fitting magnitude.

parameters. Herein, EXAFS RMC calculations incorporated the MS formalism including the scattering paths up to the fourth order. Given that the RMC technique is applied to crystalline systems with determined cell parameters, the structural parameters that we obtained are more reliable than those determined using conventional EXAFS data treatment.

The experimental and RMC-fitted  $k^2$ -weighted EXAFS spectra  $\chi(k)k^2$  and their absolute values of Fourier transforms are shown in Figure 5. A good agreement is observed between the experimental and RMC-fitted data in both the  $k$ - and  $R$ -spaces, indicating the high quality of the crystalline structures determined by XRD and their suitability for accurately

Table 1. Structural Parameters Obtained from the Fitting of the EXAFS Spectra

sample	coordination shell	coordination number (CN)	interatomic distance (R) (Å)	Debye–Waller factor ( $\sigma^2$ ) (Å <sup>2</sup> )	R-factor	interatomic distance (R) from EvAX fit (Å)	interatomic distances from XRD data (Å)
sample A	Np–O	2	1.87 ± 0.07	0.0010	R = 0.026 k range = 3–12	1.82	1.81
	Np–O	4	2.49 ± 0.01	0.0030		2.50	2.45 × 2; 2.50 × 2
	Np–O	2	2.64 ± 0.06	0.0030			2.56 × 2
	Np–C	2	3.04 ± 0.06	0.0076		2.94	2.90
	Np–C	2	3.51 ± 0.09	0.0076		3.67	3.72
	Np–Np	2	4.36 ± 0.01	0.0033		4.34	4.34
sample D	Np–O	2	1.83 ± 0.02	0.0032	R = 0.013 k range = 3–12	1.79	1.80
	Np–O	6	2.56 ± 0.01	0.0063		2.56	2.56
	Np–C	3	2.96 ± 0.02	0.0055		2.95	2.94
	Np–K	6	4.20 ± 0.30	0.0085		3.90	3.90
	Np–O	6	4.28 ± 0.10	0.0004		4.24	4.21
	Np–Np	6	5.19 ± 0.09	0.0089		5.10	5.10

reproducing the experimental EXAFS spectra. The structural parameters derived from the RMC-fitted structures are listed in Table 1. A comparison of distances from Np to its nearest neighbors shows that the RMC analysis produces interatomic with higher accuracy compared to conventional EXAFS fitting. For Samples A and D, the distance from the Np atom to the axial oxygens ( $O_{ax}$ ) is quite close, measuring 1.82 and 1.79 Å, respectively. In the  $NaNpO_2CO_3 \cdot 3H_2O$  structure, EXAFS analysis yields six equatorial oxygens ( $O_{eq}$ ) at an average distance of 2.50 Å, whereas in the  $KNpO_2CO_3$  structure,  $O_{eq}$  of Np are more ordered, with six  $O_{eq}$  atoms at 2.56 Å. The pronounced splitting of the Np–C peak was observed on the EXAFS spectra of Sample A, revealing two C atoms backscattered at 2.94 Å and two additional C atoms backscattered at 3.67 Å. This splitting suggests different functions of the O group in the  $[NpO_2CO_3]$  layer, encompassing chelating and bridge functions. The results showed good convergence in the values of the interatomic distances obtained from the XRD and EXAFS data (Table 1).

**Thermodynamic Aspects of Np(V) Carbonate Precipitation in the Presence of Na<sup>+</sup> and K<sup>+</sup>.** Conducting experiments on Np precipitation in the presence of competing cations is critical for understanding the phase that controls the Np solubility in natural waters. Samples B, C, and D were obtained in a competitive environment containing Na<sup>+</sup> and K<sup>+</sup>. The concentrations of these cations were close in the solutions used to prepare all three samples:  $[NpO_2^{+}] \approx 4 \times 10^{-3}$  M,  $[Na^{+}] \approx 7 \times 10^{-2}$  M, and  $[K^{+}] \approx 2 \times 10^{-2}$  M. There was a slight difference in the concentrations of carbonates and pH values during the precipitation of Np(V) carbonates. Specifically, Sample B was obtained at pH  $\approx$  8, while Samples C and D were prepared at pH  $\approx$  7. As mentioned above, Sample D consists of a single  $KNpO_2CO_3$  phase. Based on the XRD data, the composition of Sample B consists of 75%  $NaNpO_2CO_3 \cdot 3H_2O$  and 25%  $KNpO_2CO_3$ , while Sample C consists of 43%  $NaNpO_2CO_3 \cdot 3H_2O$  and 57%  $KNpO_2CO_3$ .

Interpreting the experimental data from a thermodynamic perspective presented certain challenges. Generally, predictions of Np speciation in solutions or solids rely on thermodynamic constants.<sup>47</sup> Herein, the solubility constants of Na- and K-containing Np carbonate phases appear to be the most important factors. Figure 6 shows the possible Np(V) chemical species that can exist in the Np(V)–Na–K carbonate system under pH 6–10. The dependencies were calculated based on available thermodynamic constants for Np solid compounds and hydrolysis complexes.<sup>49,50</sup>

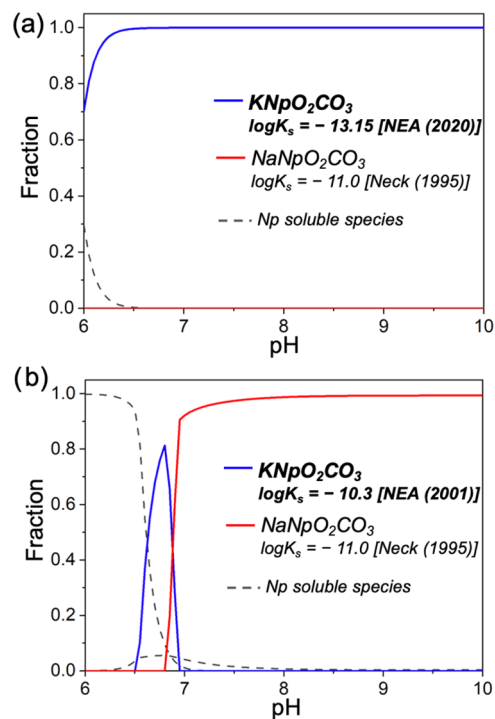


**Figure 6.** Thermodynamic modeling of Np speciation as a function of pH in a system with competing Na<sup>+</sup> and K<sup>+</sup>, calculated based on available thermodynamic constants under the following conditions:  $[Np] = 4.4 \times 10^{-3}$  M,  $[Na^{+}] = 7.0 \times 10^{-2}$  M,  $[K^{+}] = 2.2 \times 10^{-2}$  M, and  $[CO_3^{2-}] = 10^{-2}$  M. The dependencies illustrated in (a, b) were calculated using different values of the solubility constant for  $KNpO_2CO_3$  (as shown in the figure).

As reviewed in the Nuclear Energy Agency (NEA) chemical thermodynamics database, most published solubility studies indicate that hydrated  $NaNpO_2CO_3$  tends to dehydrate just above room temperature.<sup>50</sup> The amount of water in the Np(V) carbonate structure has minimal impact on its solubility constant; therefore, the variation in solubility product values for different  $NaNpO_2CO_3$  hydrated forms is insignificant.<sup>48</sup> For thermodynamic calculations shown in Figure 6, we used a solubility constant,  $\log K_s = -11.0$  (eq 1), as reported by Neck et al.<sup>31</sup>

Compared with the Na analogue, much less thermodynamic information is found for the solubility constant of  $KNpO_2CO_3$ . Some studies describe the dissolution reaction of the  $KNpO_2CO_3$  with a solubility constant,  $\log K_s = -13$ <sup>32,46,49</sup>

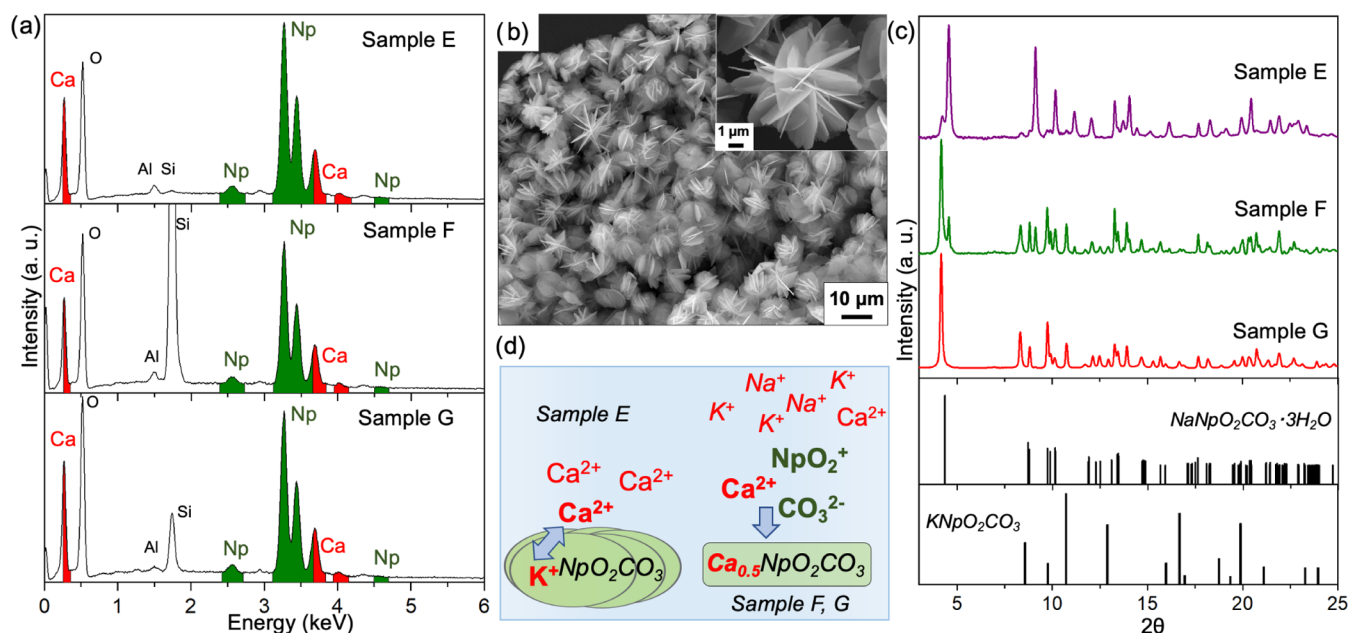
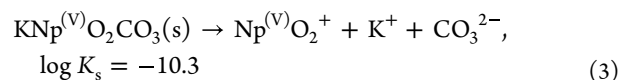
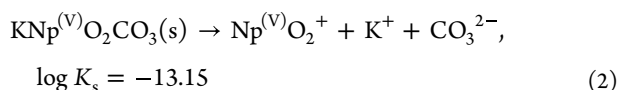
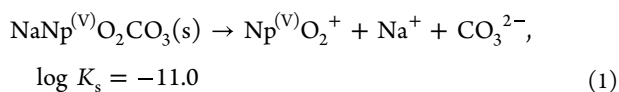


**Figure 7.** (a) EDX data for Ca-containing Np(V) carbonates. (b) SEM images of Sample G. (c) XRD patterns of Samples E–G compared to the refined structures of NaNpO<sub>2</sub>CO<sub>3</sub>·3H<sub>2</sub>O and KNpO<sub>2</sub>CO<sub>3</sub> in this study. (d) Schematic representation of Ca<sub>0.5</sub>NpO<sub>2</sub>CO<sub>3</sub> synthesis through different routes.

(eq 2). Based on this value, the thermodynamic prediction suggests that only KNpO<sub>2</sub>CO<sub>3</sub> would form under our experimental conditions (Figure 6a). However, herein, the KNpO<sub>2</sub>CO<sub>3</sub> phase precipitated only in the case of Sample D. The differences between experimental data and thermodynamic predictions may result from various experimental conditions, such as ionic strength variations and the local precipitation effect. Moreover, the experimental results imply that the thermodynamic stability of alkali-mixed Np carbonates still needs to be fully understood. Lemire et al.<sup>30</sup> reported that the nature of the solid in the Np(V)–K carbonate system changes gradually with alternations in the composition of solutions. This suggests that definitive thermodynamic parameters cannot be readily calculated from the KNpO<sub>2</sub>CO<sub>3</sub> solubility data. Consequently, the stability region of K-containing Np carbonates may be smaller than that suggested by the available thermodynamic data.

Another solubility constant for KNpO<sub>2</sub>CO<sub>3</sub>, which is  $\log K_s = -10.3$  (eq 3), has been documented in available databases.<sup>48</sup> This value considerably differs from the previous one and was estimated within the NEA based on experimental data from Visyashcheva et al.<sup>28,48</sup> Using  $\log K_s = -10.3$ , calculation of the Np fraction indicates a smaller stability region of KNpO<sub>2</sub>CO<sub>3</sub> compared to NaNpO<sub>2</sub>CO<sub>3</sub>. The impact of the pH value is substantial on the predominant Np fractions (Figure 6b). These theoretical results are consistent with the experimental data and elucidate the mixture of K- and Na-containing Np(V) phases in Samples B and C, respectively.<sup>31,48,49</sup>



**Synthesis and Characterization of Ca-Containing Np(V) Carbonates.** Understanding the behavior of Np in the presence of alkaline and alkaline earth cations is crucial for radioactive waste storage and the study of radionuclide migration. Particularly, the characteristics and potential formation of M(II)-containing neptunium carbonates are of interest, with a substantial gap in the literature regarding Np–Ca carbonates. Our study has uncovered the formation of various Ca-containing Np(V) carbonate phases under different conditions. To obtain Ca-containing Np structures, the ion exchange synthesis method was used after preparing the layered structures of K and Na carbonates (Sample E). Subsequently, we investigated whether a Ca-containing Np(V) carbonate precipitate could directly form from the solution, containing a 0.05 M CaCl<sub>2</sub> solution (Sample F) and simulated natural water (Sample G). To confirm its morphology, elemental composition, and local stoichiometry, we conducted SEM–EDX measurements on the obtained samples. In addition, this study presents XRD patterns of Ca-containing Np(V) carbonates for the first time.

According to the EDX analysis, the compound with the general chemical formula Ca<sub>0.5</sub>NpO<sub>2</sub>CO<sub>3</sub> was formed through the ion exchange reaction (Table S6). No K was detected in the solid after 3 days of ion exchange (Figure 7a), indicating the complete replacement of K<sup>+</sup> by Ca<sup>2+</sup> in the Np carbonate structure. Figure 7c shows the XRD data of Sample E in comparison with the prominent diffraction peaks of the KNpO<sub>2</sub>CO<sub>3</sub> phase, which was the initial Np phase for ion exchange (Figure 7d). XRD data revealed noticeable changes in the initial sample structure after ion exchange. It could be hypothesized that the Ca<sub>0.5</sub>NpO<sub>2</sub>CO<sub>3</sub> phase is more preferred thermodynamically than KNpO<sub>2</sub>CO<sub>3</sub> since the ion exchange reaction was successful.

Based on the EDX analysis, Samples F and G have the same chemical formula  $\text{Ca}_{0.5}\text{NpO}_2\text{CO}_3$  (Figure 7a and Table S6). Interestingly, during the precipitation of Sample G from simulated natural water, where  $\text{Ca}^{2+}$ ,  $\text{Na}^+$ ,  $\text{Mg}^{2+}$ , and  $\text{K}^+$  cations were present in comparable concentrations, only Ca was absent in the sediment. SEM micrographs of Sample F shown in Figure 7b reveal that it consists of nanoplates with a thickness of 50–100 nm and a diameter of  $\sim 5 \mu\text{m}$ . These plates assemble into flower-like structures, resembling the K and Na phases of Np carbonate discussed earlier (Figure 2a,b).

Figure 7c shows the XRD patterns of Ca-containing Np carbonate samples synthesized under different synthesis conditions. Despite having identical chemical compositions, samples E–G exhibit different structures. Based on the distribution of diffraction maxima, Sample G appears to be a single-phase sample, with a crystal structure resembling that of the previously discussed  $\text{NaNpO}_2\text{CO}_3 \cdot 3\text{H}_2\text{O}$  carbonate. The XRD pattern of Sample G is best described in the orthorhombic-P unit cell with cell parameters  $a = 10.33 \text{ \AA}$ ,  $b = 4.33 \text{ \AA}$ , and  $c = 4.88 \text{ \AA}$  (Figure S6a). The presence of the  $4.33 \text{ \AA} \times 4.88 \text{ \AA}$  plane in the Sample G structure, as in Sample A, indicates the preservation of the Na-type neptunyl layer  $[\text{NpO}_2\text{CO}_3]_n^{n-}$ . In Sample E, the Ca-containing Np carbonate phase is dominated by another crystal structure. The XRD pattern of Sample E is best described in an I-centered orthorhombic cell with cell parameters  $a = 18.85 \text{ \AA}$ ,  $b = 4.88 \text{ \AA}$ , and  $c = 4.34 \text{ \AA}$  (Figure S6b). This phase also contains a  $4.34 \text{ \AA} \times 4.88 \text{ \AA}$  plane, indicating the Na-type neptunyl layer  $[\text{NpO}_2\text{CO}_3]_n^{n-}$ . Sample F appears to be a mixture of Samples E and G.

The presence of a Na-type neptunyl layer in the structure of Ca/Np mixed carbonates is intriguing, particularly as  $\text{K}^+$  to  $\text{Ca}^{2+}$  exchange reactions transform the Np carbonate anionic layer structure from hexagonal to orthorhombic. This aligns with the existing literature that suggests cation radius affects the anionic layer structure. Large cations (K,  $\text{NH}_4^+$ , etc.) form mixed Np(V) carbonates with a hexagonal neptunyl layer,<sup>18,22,23,27,28</sup> while small cations ( $\text{Na}^+$  and  $\text{Li}^+$ ) form mixed Np(V) carbonates with an orthorhombic anionic layer.<sup>21,25</sup> The radius of  $\text{Ca}^{2+}$  (1.00  $\text{ \AA}$ ) is close to that of  $\text{Na}^+$  (1.02  $\text{ \AA}$ ), supporting this theory.<sup>50</sup> Coordination numbers (CNs) are known to depend on ionic radii.<sup>50</sup> Based on the structure models of nonhydrated Na- and K-containing Np carbonates proposed herein and the literature, the CN of a cation in the anionic interlayer space can be 7 and 12, respectively.<sup>21,32</sup> Thus, orthorhombic-type neptunyl layers form with small cations, while hexagonal-type neptunyl layers favor large ones. Hydrated orthorhombic-type Np(V) carbonates could have water molecules within their interlayer space,<sup>20,25</sup> forming hydrogen bonds with O, shifting layers and producing various structural forms, such as  $\text{NaNpO}_2\text{CO}_3 \cdot 3\text{H}_2\text{O}$ , as discussed herein, or  $\text{LiNpO}_2\text{CO}_3 \cdot 2\text{H}_2\text{O}$ , as discussed by Charushnikova et al.<sup>25</sup>

Investigating the structures and thermodynamics of  $\text{M}^{(\text{II})}_{0.5}\text{NpO}_2\text{CO}_3$  compounds with various divalent cations is crucial owing to the observed formation of the stable  $\text{Ca}_{0.5}\text{NpO}_2\text{CO}_3$  phase under a wide range of conditions. These compounds may have a noticeable impact on Np speciation in the environment, potentially more so than the  $\text{M}^{(\text{I})}\text{NpO}_2\text{CO}_3$  phases. The discussion of thermodynamic data for  $\text{M}^{(\text{I})}\text{NpO}_2\text{CO}_3$  and  $\text{M}^{(\text{II})}_{0.5}\text{NpO}_2\text{CO}_3$ , combined with structural studies, is necessary for an adequate prediction of the thermodynamically stable phase under environmental

conditions, which are vital for modeling and creating storage facilities. Moreover, all trends discussed earlier are particularly relevant in the context of the analogy between Np(V) and Pu(V), another highly radioactive actinide. Structural data on Pu-containing solids are even scarcer than those for Np. However, it has already been shown that the structures of K- and  $\text{NH}_4^+$ -containing Pu(V) and Np(V) mixed carbonates coincide.<sup>18,23,51</sup> Consequently, the study of Np(V) mixed carbonates would help to understand the potential formation and crystal structures of Pu(V) mixed carbonates with both M(I) and M(II) cations.

## CONCLUSIONS

Herein, the synthesis and characterization of different cation-mixed Np carbonate phases were thoroughly explored. Detailed information about the composition, morphology, and structure of hydrated Na-, K-, and Ca-containing Np(V) carbonates was obtained. SEM images revealed the formation of flower-like microstructures in the synthesized Np(V) carbonate samples. The XRD data revealed that hydrated  $\text{NaNpO}_2\text{CO}_3$  crystallized in the triclinic *P1* space group, consisting of layers  $[\text{NpO}_2\text{CO}_3]$ , with solvated  $\text{Na}^+$  within the interlayer space, resulting in a trihydrate structure,  $\text{NaNpO}_2\text{CO}_3 \cdot 3\text{H}_2\text{O}$ . The Np–Na carbonate structure was analyzed through TG–DSC, confirming the presence of crystallization water. In contrast, the  $\text{KNpO}_2\text{CO}_3$  carbonate exhibited a hexagonal *P6<sub>3</sub>/mmc* space group, consistent with the literary. To the best of our knowledge, the local atomic environment of Np in the structures of  $\text{NaNpO}_2\text{CO}_3$  and  $\text{KNpO}_2\text{CO}_3$  has been achieved for the first time. The interatomic distances calculated from XRD and EXAFS data were in good agreement, highlighting the reliability of the structural information. Therefore, the splitting of the Np–C coordination sphere in the  $\text{NaNpO}_2\text{CO}_3 \cdot 3\text{H}_2\text{O}$  structure resulted from a different function of O in the carbonate group. Thermodynamic predictions on Np(V) phase formation in the presence of  $\text{K}^+$  and  $\text{Na}^+$  vary considerably depending on the solubility product constants used. Experimental results indicated that the solubility product constants for the hydrated  $\text{NaNpO}_2\text{CO}_3$  and  $\text{KNpO}_2\text{CO}_3$  phases are similar. During Np(V) precipitation in carbonate-reached media with  $\text{Na}^+$  and  $\text{K}^+$  at neutral pH, a mixture of  $\text{NaNpO}_2\text{CO}_3$  and  $\text{KNpO}_2\text{CO}_3$  is formed with a high probability. However, during Np(V) precipitation in carbonate media with competing  $\text{Na}^+$ ,  $\text{K}^+$ , and  $\text{Ca}^{2+}$ , a Ca-containing Np(V) carbonate is formed. Moreover, the compound  $\text{Ca}_{0.5}\text{NpO}_2\text{CO}_3$  could be easily obtained via ion exchange with a  $\text{KNpO}_2\text{CO}_3$  substrate. These experimental results underscore the high thermodynamic stability of  $\text{Ca}_{0.5}\text{NpO}_2\text{CO}_3$  and emphasize the need for further investigation in this direction.

## ASSOCIATED CONTENT

### Supporting Information

The Supporting Information is available free of charge at <https://pubs.acs.org/doi/10.1021/acs.inorgchem.3c02737>.

UV–vis data; synthesis conditions; XANES spectra; SEM–EDX data; crystallographic data for sample A and sample D; and experimental diffraction pattern of samples G and samples E with refined peak positions and calculated cell parameters (PDF)

## Accession Codes

CCDC 2268095–2268096 contain the supplementary crystallographic data for this paper. These data can be obtained free of charge via [www.ccdc.cam.ac.uk/data\\_request/cif](http://www.ccdc.cam.ac.uk/data_request/cif), by emailing [data\\_request@ccdc.cam.ac.uk](mailto:data_request@ccdc.cam.ac.uk), or by contacting The Cambridge Crystallographic Data Centre, 12 Union Road, Cambridge CB2 1EZ, UK; fax: +44 1223 336033.

## AUTHOR INFORMATION

### Corresponding Author

Tatiana V. Plakhova – Lomonosov Moscow State University, 119991 Moscow, Russia; [orcid.org/0000-0001-8286-9241](https://orcid.org/0000-0001-8286-9241); Email: [Tatiana.v.plakhova@gmail.com](mailto:Tatiana.v.plakhova@gmail.com)

### Authors

Anastasiia S. Kuzenkova – Lomonosov Moscow State University, 119991 Moscow, Russia

Iurii M. Nevolin – Lomonosov Moscow State University, 119991 Moscow, Russia; Frumkin Institute of Physical Chemistry and Electrochemistry, Russian Academy of Sciences, 119071 Moscow, Russia

Elizaveta S. Kulikova – National Research Centre «Kurchatov Institute», 123182 Moscow, Russia

Alexander L. Trigub – Lomonosov Moscow State University, 119991 Moscow, Russia; National Research Centre «Kurchatov Institute», 123182 Moscow, Russia

Vasiliy O. Yapaskurt – Lomonosov Moscow State University, 119991 Moscow, Russia

Maria D. Shaulskaya – Lomonosov Moscow State University, 119991 Moscow, Russia

Dmitry M. Tsybarenko – Lomonosov Moscow State University, 119991 Moscow, Russia; [orcid.org/0000-0002-2818-5639](https://orcid.org/0000-0002-2818-5639)

Anna Yu. Romanchuk – Lomonosov Moscow State University, 119991 Moscow, Russia; [orcid.org/0000-0002-7805-8670](https://orcid.org/0000-0002-7805-8670)

Stepan N. Kalmykov – Lomonosov Moscow State University, 119991 Moscow, Russia

Complete contact information is available at:

<https://pubs.acs.org/10.1021/acs.inorgchem.3c02737>

### Author Contributions

A.S.K., T.V.P., and A.Yu.R. conceived, designed, and performed the experiments. E.S.K. performed PXRD measurements. M.D.S. and D.M.T. processed PXRD data. I.M.N. performed TG–DSC measurements. V.O.Y. performed SEM–EDX measurements. A.L.T. performed EXAFS measurements and processed data. T.V.P., A.S.K., D.M.T., A.Yu.R., and S.N.K. discussed the results and co-wrote the paper.

### Funding

Russian Science Foundation, grant No. 22–73–10056.

### Notes

The authors declare no competing financial interest.

## ACKNOWLEDGMENTS

The study was supported by the Russian Science Foundation (grant No. 22-73-10056). Experimental studies were partially performed on equipment acquired with the funding of M.V. Lomonosov Moscow State University Program of Development and the Core Facilities Center of IPCE RAS (CKP FMI IPCE RAS). Experimental studies at the Kurchatov Synchrotron Radiation Center performed with the financial support of

the Ministry of Science and Higher Education of the Russian Federation within the framework of the agreement on the provision of grants from the federal budget in the form of subsidies dated December 22, 2021 No. 075-11-2021-086 (identifier of the state contract No 000000S507521RN60002). EXAFS spectra fitting has been carried out using computing resources of the federal collective usage centre Complex for Simulation and Data Processing for Mega-science Facilities at NRC “Kurchatov Institute”, <http://ckp.nrcki.ru/>. We thank Ivan V. Mikheev and Yuri A. Teterin Jr., for their valuable experimental help.

## ABBREVIATIONS

XRD, X-ray diffraction; XAS, X-ray absorption spectroscopy; EXAFS, extended X-ray absorption fine structure spectroscopy; XANES, X-ray absorption near-edge structure; CN, coordination number; TG–DSC, thermogravimetry and differential scanning calorimetry; SEM, scanning electron microscopy; EDX, energy-dispersive X-ray analysis

## REFERENCES

- (1) Ewing, R. C.; Whittleston, R. A.; Yardley, B. W. D. Geological Disposal of Nuclear Waste: A Primer. *Elements* **2016**, *12* (4), 233–237.
- (2) Alexander, W. R.; McKinley, L. E. *Deep Geological Disposal of Radioactive Waste*; Elsevier, 2007; Vol. 9.
- (3) International Atomic Energy Agency. *Scientific and Technical Basis for the Geological Disposal of Radioactive Wastes*, Technical Reports Series; International atomic energy agency: Vienna, 2003; Vol. 413.
- (4) Peruski, K. M.; Maloubier, M.; Kaplan, D. I.; Almond, P. M.; Powell, B. A. Mobility of Aqueous and Colloidal Neptunium Species in Field Lysimeter Experiments. *Environ. Sci. Technol.* **2018**, *52* (4), 1963–1970.
- (5) Romanchuk, A. Y.; Vlasova, I. E.; Kalmykov, S. N. Speciation of Uranium and Plutonium From Nuclear Legacy Sites to the Environment: A Mini Review. *Front. Chem.* **2020**, *8*, No. 630.
- (6) Neumann, T. Fundamentals of Aquatic Chemistry Relevant to Radionuclide Behaviour in the Environment. In *Radionuclide Behaviour in the Natural Environment*; Elsevier, 2012; pp 13–43.
- (7) Altmaier, M.; Vercouter, T. Aquatic Chemistry of the Actinides: Aspects Relevant to Their Environmental Behavior. In *Radionuclide Behaviour in the Natural Environment*; Elsevier, 2012; pp 44–69.
- (8) Bruno, J.; Delos, A. Safety Assessment of Nuclear Waste Repositories: A Radionuclide Migration Perspective. In *Radionuclide Behaviour in the Natural Environment*; Elsevier, 2012; pp 646–692.
- (9) Yoshida, Z.; Johnson, S. G.; Kimura, T.; Krsul, J. R. Neptunium. In *The Chemistry of the Actinide and Transactinide Elements*; Springer Netherlands: Dordrecht, 2008; pp 699–812.
- (10) Christiansen, B. C.; Geckeis, H.; Marquardt, C. M.; Bauer, A.; Römer, J.; Wiss, T.; Schild, D.; Stipp, S. L. S. Neptunyl (NpO<sup>2+</sup>) Interaction with Green Rust, GRNa<sub>2</sub>SO<sub>4</sub>. *Geochim. Cosmochim. Acta* **2011**, *75* (5), 1216–1226.
- (11) Clark, D. L.; Conradson, S. D.; Ekberg, S. A.; Hess, N. J.; Neu, M. P.; Palmer, P. D.; Runde, W.; Tait, C. D. EXAFS Studies of Pentavalent Neptunium Carbonate Complexes. Structural Elucidation of the Principal Constituents of Neptunium in Groundwater Environments. *J. Am. Chem. Soc.* **1996**, *118* (8), 2089–2090.
- (12) Petrov, V. G.; Fellhauer, D.; Gaona, X.; Dardenne, K.; Rothe, J.; Kalmykov, S. N.; Altmaier, M. Solubility and Hydrolysis of Np(V) in Dilute to Concentrated Alkaline NaCl Solutions: Formation of Na-Np(V)-OH Solid Phases at 22 °C. *Radiochim. Acta* **2017**, *105* (1), 1–20.
- (13) Fellhauer, D.; Altmaier, M.; Gaona, X.; Lützenkirchen, J.; Fanghänel, T. Np(V) Solubility, Speciation and Solid Phase Formation in Alkaline CaCl<sub>2</sub> Solutions. Part II: Thermodynamics

and Implications for Source Term Estimations of Nuclear Waste Disposal. *Radiochim. Acta* **2016**, *104* (6), 381–397.

(14) Rai, D.; Ryan, J. Neptunium(IV) Hydrate Oxide Solubility under Reducing and Carbonate Conditions. *Inorg. Chem.* **1985**, *24* (3), 247–251.

(15) Bidoglio, G.; Tanet, G.; Chatt, A. Studies on Neptunium (V) Carbonate Complexes under Geologic Repository Conditions. *Radiochim. Acta* **1985**, *38*, 21–26.

(16) Fellhauer, D.; Lee, J.-Y.; DiBlasi, N. A.; Walter, O.; Gaona, X.; Schild, D.; Altmaier, M. Crystal Structure and Stability in Aqueous Solutions of  $\text{Na}_{0.5}[\text{NpO}_2(\text{OH})_{1.5}] \cdot 0.5\text{H}_2\text{O}$  and  $\text{Na}[\text{NpO}_2(\text{OH})_2]$ . *J. Am. Chem. Soc.* **2022**, *144* (21), 9217–9221.

(17) Heberling, F.; Denecke, M. A.; Bosbach, D. Neptunium(V) Coprecipitation with Calcite. *Environ. Sci. Technol.* **2008**, *42* (2), 471–476.

(18) Keenan, T. K.; Kruse, F. H. Potassium Double Carbonates of Pentavalent Neptunium, Plutonium, and Americium. *Inorg. Chem.* **1964**, *3* (9), 1231–1232.

(19) Nigon, J. P.; Penneman, R. A.; Staritzky, E.; Keenan, T. K.; Asprey, L. B. Alkali Carbonates of Np(V), Pu(V) and Am(V). *J. Phys. Chem. A* **1954**, *58* (5), 403–404.

(20) Volkov, Y. F.; Visyashcheva, G. I.; Kapshukov, I. I. Production and Identification of Hydrate Forms of Sodium Monocarbonate-neptunaylate. *Radiokhimiya* **1977**, *19*, 319–323.

(21) Volkov, Y. F.; Tomilin, S. V.; Visyashcheva, G. I.; Kapshukov, I. I. X-Ray Structure Analysis of  $\text{LiNpO}_2\text{CO}_3$  and  $\text{NaNpO}_2\text{CO}_3$ . *Radiokhimiya* **1979**, *21*, 668–672.

(22) Volkov, Y. F.; Kapshukov, I. I.; Visyashcheva, G. I.; Yakovlev, G. N. X-Ray Investigation of Neptunium (V), Plutonium (V), and Americium (V) Monocarbonates with Potassium. *Radiokhimiya* **1974**, *16*, 863–867.

(23) Nevolin, I. M.; Petrov, V. G.; Grigoriev, M. S.; Averin, A. A.; Shiryayev, A. A.; Krot, A. D.; Maslakov, K. I.; Teterin, Y. A.; Fedoseev, A. M. Crystal Structure of Mixed Np(V)-Ammonium Carbonate. *Symmetry* **2022**, *14* (12), No. 2634.

(24) Grigor'ev, M. S.; Budantseva, N. A.; Fedoseev, A. M. Study of the Monocarbonate Complex of Pentavalent Neptunium ( $\text{NH}_4$ )- $[\text{NpO}_2(\text{CO}_3)]$ . *Russ. J. Coord. Chem.* **2010**, *36* (2), 157–160.

(25) Charushnikova, I. A.; Krot, N. N.; Polyakova, I. N. Crystal Structure of Double Lithium Neptunium(V) Carbonate Dihydrate  $\text{LiNpO}_2\text{CO}_3 \cdot 2\text{H}_2\text{O}$ . *Radiokhimiya* **2004**, *46* (4), 315–317.

(26) Volkov, Y. F.; Visyashcheva, G. I.; Tomilin, S. V.; Kapshukov, I. I.; Rykov, A. G. Study of Carbonate Compounds of Pentavalent Actinides with Alkali-Metal Cations: X. Composition and Crystal Structure of Carbonates. *Radiokhimiya* **1981**, *23*, 200–204.

(27) Volkov, Y. F.; Visyashcheva, G. I.; Kapshukov, I. I.; Simakin, G. A.; Yakovlev, G. N. Composition and Properties of Carbonates of the Pentavalent Actinides. *Radiokhimiya* **1976**, *18*, 96–100.

(28) Visyashcheva, G. I.; Volkov, Y. F.; Simakin, G. A.; Kapshukov, I. I.; Bezv, A. S.; Yakovlev, G. N. Carbonate Compounds of Pentavalent Actinides with Alkali Metal Cations: I. Composition and Some Properties of Solid Carbonates of Pentavalent Neptunium with Potassium Obtained from  $\text{K}_2\text{CO}_3$  Solutions. *Radiokhimiya* **1974**, *16*, 832–837.

(29) Maya, L. Hydrolysis and Carbonate Complexation of Dioxoneptunium(V) in 1.0 M Sodium Perchlorate at 25.degree.C. *Inorg. Chem.* **1983**, *22* (14), 2093–2095.

(30) Lemire, R. J.; Boyer, G. D.; Campbell, A. B. The Solubilities of Sodium and Potassium Dioxoneptunium(V) Carbonate Hydrates at 30, 50 and 75°C. *Radiochim. Acta* **1993**, *61*, 57–63.

(31) Neck, V.; Runde, W.; Kim, J. I. Solid-Liquid Equilibria of Neptunium(V) in Carbonate Solutions of Different Ionic Strengths: II. Stability of the Solid Phases. *J. Alloys Compd.* **1995**, *225* (1–2), 295–302.

(32) Vitova, T.; Pidchenko, I.; Schild, D.; Prüßmann, T.; Montoya, V.; Fellhauer, D.; Gaona, X.; Bohnert, E.; Rothe, J.; Baker, R. J.; Geckeis, H. Competitive Reaction of Neptunium(V) and Uranium(VI) in Potassium-Sodium Carbonate-Rich Aqueous Media: Spec-

iation Study with a Focus on High-Resolution X-Ray Spectroscopy. *Inorg. Chem.* **2020**, *59* (1), 8–22.

(33) Svetogorov, R. D.; Dorovatovskii, P. V.; Lazarenko, V. A. Belok/XSA Diffraction Beamline for Studying Crystalline Samples at Kurchatov Synchrotron Radiation Source. *Cryst. Res. Technol.* **2020**, *55* (5), No. 1900184.

(34) Svetogorov, R. D. Computer Program “Dionis Diffraction Open Integration Software” Certificate of State Registration No. 2018660965 RF. Application No. 2018618585; Dec. 08/10/2018; Publ. 08/30/2018.

(35) Prescher, C.; Prakapenka, V. B. DIOPTAS: A Program for Reduction of Two-Dimensional X-Ray Diffraction Data and Data Exploration. *High Pressure Res.* **2015**, *35* (3), 223–230.

(36) Louër, D.; Louër, M. Méthode d'essais et Erreurs Pour l'indexation Automatique Des Diagrammes de Poudre. *J. Appl. Crystallogr.* **1972**, *5* (4), 271–275.

(37) Coelho, A. A. Indexing of Powder Diffraction Patterns by Iterative Use of Singular Value Decomposition. *J. Appl. Crystallogr.* **2003**, *36* (1), 86–95.

(38) Petricek, V.; Dusek, M.; Palatinus, L. *Jana2006. Structure Determination Software Programs*; Institute of Physics: Praha, Czech Republic, 2006.

(39) Ellinger, F. H.; Zachariasen, W. H. The Crystal Structure of  $\text{KPuO}_2\text{CO}_3$ ,  $\text{NH}_4\text{PuO}_2\text{CO}_3$  and  $\text{RbAmO}_2\text{CO}_3$ . *J. Phys. Chem. A* **1954**, *58*, 405–408.

(40) Favre-Nicolin, V.; Černý, R. FOX, ‘free Objects for Crystallography’: A Modular Approach to *Ab Initio* Structure Determination from Powder Diffraction. *J. Appl. Crystallogr.* **2002**, *35* (6), 734–743.

(41) Chernyshov, A. A.; Veligzhanin, A. A.; Zubavichus, Y. V. Structural Materials Science End-Station at the Kurchatov Synchrotron Radiation Source: Recent Instrumentation Upgrades and Experimental Results. *Nucl. Instrum. Methods Phys. Res., Sect. A* **2009**, *603* (1–2), 95–98.

(42) Newville, M. EXAFS Analysis Using FEFF and FEFFIT. *J. Synchrotron Radiat.* **2001**, *8*, 96–100.

(43) Ankudinov, A. L.; Ravel, B.; Rehr, J. J.; Conradson, S. D. Real-Space Multiple-Scattering Calculation and Interpretation of x-Ray-Absorption near-Edge Structure. *Phys. Rev. B* **1998**, *58*, 7565–7576.

(44) Timoshenko, J.; Kuzmin, A.; Purans, J. EXAFS Study of Hydrogen Intercalation into  $\text{ReO}_3$  Using the Evolutionary Algorithm. *J. Condens. Matter Phys.* **2014**, *26* (5), No. 055401.

(45) Timoshenko, J.; Kuzmin, A. Wavelet Data Analysis of EXAFS Spectra. *Comput. Phys. Commun.* **2009**, *180* (6), 920–925.

(46) Novak, C. F.; Ilham, A. M.; Becraft, K. A.; Carpenter, S. A.; Hakem, N.; Prussin, T. Measurement and Thermodynamic Modeling of Np(V) Solubility in Aqueous  $\text{K}_2\text{CO}_3$  Solutions to High Concentrations. *J. Solution Chem.* **1997**, *26* (7), 681–697.

(47) Vitorge, P.; Capdevila, H. Thermodynamic Data for Modelling Actinide Speciation in Environmental Waters. *Radiochim. Acta* **2003**, *91*, 623–631.

(48) Lemire, R. J.; Fuger, J.; Spahiu, K.; Sullivan, J. C.; Nitsche, H.; Ullman, W. J.; Potter, P.; Vitorge, P.; Rand, M. H.; Wanner, H.; Rydberg, J. *NEA, Chemical Thermodynamics of Neptunium and Plutonium*; OECD Publishing: Paris, 2001.

(49) Grenthe, I.; Plyasunov, A. V.; Runde, W. H.; Grambow, B.; Konings, R. J. M.; Smith, A. L.; Moore, E. E.; Martinez, J. S.; Costa, D. *NEA, Second Update on the Chemical Thermodynamics of U, Np, Pu, Am. and Tc*; OECD Publishing: Paris, 2020.

(50) Shannon, R. D. Revised Effective Ionic Radii and Systematic Studies of Interatomic Distances in Halides and Chalcogenides. *Acta Crystallogr. A* **1976**, *32* (5), 751–767.

(51) Kvashnina, K. O.; Romanchuk, A. Y.; Pidchenko, I.; Amidani, L.; Gerber, E.; Trigub, A.; Rossberg, A.; Weiss, S.; Popa, K.; Walter, O.; Caciuffo, R.; Scheinost, A. C.; Butorin, S. M.; Kalmykov, S. N. A Novel Metastable Pentavalent Plutonium Solid Phase on the Pathway from Aqueous Plutonium(VI) to  $\text{PuO}_2$  Nanoparticles. *Angew. Chem., Int. Ed.* **2019**, *58* (49), 17558–17562.